Slow Slip Events: Earthquakes in Slow Motion

Sylvain Michel[1, 2,*], Adriano Gualandi[1,3], Jean-Philippe Avouac[1],

[1] California Institute of Technology, Department of Geology and Planetary Sciences, 1200 E California Blvd, Pasadena, CA, 91125, USA

[2]University of Cambridge, Department of Earth Sciences, Bullard Laboratories, Madingley Road, Cambridge, Cambridgeshire, CB3 0EZ, UK

[3] Jet Propulsion Laboratory, California Institute of Technology, 4800 Oak Grove Dr, Pasadena, CA, 91109, USA

* Now at Laboratoire de Géologie, Ecole Normale Supérieure, 24 Rue Lhomond, 75005, Paris, France.

Faults can slip episodically during earthquakes, but also during transient aseismic slip events[1-7], often called Slow Slip Events (SSEs). Previous studies based on observations compiled from various tectonic settings[8-10] have suggested that the moment of SSEs is proportional to their duration, T, instead of the $M_0 \propto T^3$ scaling found for earthquakes[11,12]. This finding has spurred efforts to unravel the cause for this difference of scaling [8,13-17]. Thanks to a new catalog of SSEs on the Cascadia megathrust based on the inversion of surface deformation measurements between 2007 and 2017[18], we find that a cubic moment-duration scaling law is more likely. Like regular earthquakes, SSEs also obey $M_0 \propto A^{3/2}$, where *A* is the rupture area, and the Gutenberg-Richter frequency-magnitude relationship. Finally, these SSE slip models show pulse-like ruptures similar to seismic

ruptures. The dynamic and scaling properties of SSEs are thus strikingly similar to those of regular earthquakes.

Geodetic monitoring of strain accumulation and release along various subduction zones has revealed episodic events of aseismic slip along different megathrusts[1-5]. These Slow Slip Events (SSEs) are typically accompanied by a burst of weak low-frequency seismic signals called tremors[19,20]. The characteristics of these slow earthquakes compiled from different subduction zones[8] suggest that their moment, M_0 (defined as the integral of slip over the fault area multiplied by the shear modulus), is proportional to their duration, T. It has therefore been inferred that SSEs and earthquakes, which obey[12] $M_0 \propto T^3$, correspond to distinct modes of slip[8]. The cubic scaling is expected for circular ruptures with constant stress drop expanding at a constant rate[12], a kinematic model close to the dynamic circular crack model[21] which fits most properties of earthquakes to first order. The Moment-duration scaling should however transition to $M_0 \propto T$ for the larger 'bounded' ruptures that saturate the seismogenic zone[13]. This transition is hardly seen in seismicity catalogs as they are dominated by smaller, unbounded events[13,22]. By contrast, only the larger SSEs are generally detected with geodetic techniques and they generally show large aspect ratios suggesting bounded ruptures. This consideration lead to the suggestion[13] that the different scaling between regular earthquakes and SSEs arises because earthquakes catalogs are dominated by unbounded ruptures while SSEs mostly represent bounded ruptures. An alternative view is that the difference of scaling between earthquakes and SSEs reflects a fundamentally different dynamics[8,17].

In this study we take advantage of a recent catalog of SSEs from Cascadia[18] which was obtained from the inversion of geodetic position time series recorded at 352 continuous GPS stations between 2007.000 and 2017.632. After extracting a secular trend average through the SSEs from the time series, and deducing from it the pattern of locking along the plate interface (Fig. 1), the data were corrected for the effect of surface loads as well as of co- and post-seismic slip. These corrected time series were used to image spatio-temporal variations of slip along the megathrust (Fig. 1). The catalog of SSEs extracted from the slip model history on the whole megathrust contains 64 events which were found to coincide with the spatio-temporal distribution of tremors (Fig. 2), as was found in previous similar studies[23,24]. Individual events show unidirectional or bidirectional ruptures with a rupture front velocity between ~5.5 km/day and ~11 km/day[18]. The larger ones show pulse-like behavior very similar to large earthquake ruptures[25] but with a much lower propagation and slip rates. Figure 1 shows the cumulated distribution of slip resulting from all 64 SSEs. As shown by Gao and Wang[26], the zone of episodic slow slip and tremors follows closely the intersection of the forearc Moho with the megathrust, and is separated from the shallower locked zone by a 40 km wide band of steady creep (Fig. 1). The catalog contains SSEs with a relatively wide range of sizes spanning moment magnitudes between $\sim M_w$ 5.3 and M_w 6.8 (Fig. 2), allowing for the investigation of the scaling properties of a population of SSEs which all happened in relatively narrow range of conditions.

The moment-duration data of this catalog falls in the slow-slip domain identified by Ide et al.[8] (red shading in Fig. 3 and S1). However they don't follow the linear scaling proposed in that study, and align better along the $M_0 \propto T^3$ scaling of earthquakes. This dataset suffers however from a bias since a low-pass temporal filter with a cut-off period of ~30 days was applied to the time series. To refine the analysis and alleviate the possibility of a bias introduced by the automatic picking of the onset and end of the SSEs, we carried out manual measurements using time series filtered with a shorter cut-off period of ~9 days, (see

Supplements for details). For sanity we removed 17 events which we considered questionable, and combined 7 pairs of events, due to their closeness in time and space. The final revised catalog consists of 40 events. For each event we estimate minimum and maximum durations and find the same trend as the original catalog. We next use the revised dataset to search for the best fitting scaling law, taking into account duration and magnitude uncertainties and the effect of the filter (see Methods for details). For example we show in Figure 3a where filtered data should plot if $M_0 \propto T$ (yellow dots) and $M_0 \propto T^3$ (green dots) were the true relationships to generate the observations. The RMSE for c=3 is about half the value obtained for c=1 and varies little for c≥3. So we conclude that SSEs occurring under a narrow range of conditions (*e.g.*, temperature and pressure), as is the case in the deep SSEs from Cascadia analyzed here, follow a near cubic moment-duration scaling like regular earthquakes. This finding is all the more unexpected since most of the SSEs in our catalog ruptured the entire width of the zone of episodic slow slip and tremors defined from the cumulated slip (Figs. 1&S4) and have large aspect ratios (Fig. 4). They would therefore be expected to follow a linear scaling[13]. It is noteworthy that, while the cubic scaling of regular earthquake is generally justified based on the circular crack model[27], the same scaling is observed in our dataset where most ruptures are very elongated with aspect ratios of 2 to 12 (Fig 4b).

The original catalog as well as our manual measurement also define a tightly constrained moment-rupture area scaling following approximately the $M_0 \propto A^{3/2}$ scaling of regular earthquakes (the best fitting scaling law exponent is actually 1.25, see Supplements for details) (Fig. 3f). The ratio $M_0/A^{3/2}$ is however three orders of magnitude smaller, implying a stress drop of ~4.3±2.0 kPa, based on the same circular crack model generally used to quantify seismic ruptures[12], *vs* 1-10MPa for regular earthquakes. This means stress drop is however questionable as the rupture areas are quite elongated (Fig. 4b). We therefore estimated the average stress drop for each of our SSE based on our slip model using the approach of Noda et al.[28] and using Meade's analytical solution[29] for triangular sub-faults. The values range between 0.9 and 18.0 kPa, with a mean of ~5.8 kPa and a standard deviation of 2.0 kPa. Our mean stress drop is about 10 times lower than the value proposed by Schmidt and Gao[30] based on the slip model of 16 M_w 6.2-6-7 events between 1998 and 2008. Given that the slip-distributions are similar (the three common events are compared in the Supplements), we suspect that this difference is due to the way rupture area were measured by Schmidt and Gao[30], the fact that our slip models do not account for the slip that would be needed to balance interseismic loading during SSE, and the possibility that our slip models are smoother due to stronger regularization.

We also examined the SSEs frequency-magnitude scaling (Fig. 4a). We show the distributions obtained from both the original catalog and the revised catalog. The data selection in the revised catalog results in a roll-over at lower magnitudes, but in any case we find that the SSEs approximately obey the Gutenberg-Richter relationship with a b-value of the order of ~0.8. The abrupt drop in the frequency of events larger than M_w 6.4 suggests a truncation effect. The truncation cannot be explained by the transition from unbounded ruptures to bounded ruptures in width (this transition would occur at a much lower magnitude $\sim M_w$ 5.7 given the aspect ratio of the ruptures), but it could alternatively be due to the along-strike segmentation discussed below. With only 11 events with M_w>6.4, this observation should however be considered with caution. A previous study had also argued for SSEs obeying the Gutenberg-Richter law[31] but used moment inferred from duration assuming linear proportionality. It seems that the conclusion holds in spite of this probably incorrect scaling assumption.

Finally, we note that the zone of SSEs can be divided into a discrete number of segments that slip systematically as a whole, either independently or jointly (Fig. 2). From the rupture patterns, cumulative slip distribution, and number of time a sub-fault has slipped (Fig. S4), we defined 13 segments (Fig. 2). Segments 1 and 2 are extremely coupled. They mostly rupture together expect for a rupture in July 2014 (2014.612) which was restricted to segment 2. Segment 7 ruptured in combination with segments 6 and 8 in 2014, but never by itself. The segmentation of the Cascadia SSE zone had already been noticed[9], and a similar segmentation is observed in Japan[32]. This segmentation is qualitatively similar to the segmentation defined by regular megathrust earthquakes[33,34].

In conclusion, the $M_0 \propto T$ scaling proposed in the seminal study of Ide et al.[8], probably arises from the assembling of slow slip events occurring under different conditions. We suspect that, as described here for the particular case of the SSEs in Cascadia, any subset of SSEs under similar conditions would yield a cubic scaling law as we found here. The along-strike segmentation, frequency-magnitude distribution, and scaling properties of SSEs on the Cascadia subduction zone are thus found to be remarkably similar to those of regular earthquakes. The pulse-like propagation of individual events also looks very similar to the seismic ruptures as inferred for large SSEs in the context of the Mexican subduction[35]. We infer that the dynamics governing aseismic SSEs is not that different from the dynamics governing seismic ruptures, a surprising result given that seismic ruptures are commonly thought to be governed by inertial effects which should not play any role in the case for SSEs. Unexpectedly, our results also call for reexamination of the cause of the $M_0 \propto A^{3/2}$ scaling as it seems that, at least in the case of SSEs, the explanation based on the circular crack model would not hold. It also calls for a reexamination of the effect of geometric bounding on scaling properties of regular earthquakes as well as SSEs. The similar scaling properties of SSEs and regular earthquakes suggest that SSEs might help develop and test dynamic models of earthquake sequences which are difficult to constrain from observations due in particular to the long return period of large earthquakes.

1 Dragert, H., Wang, K. & James, S. T. A silent slip event on the deeper Cascadia subduction interface. *Science* **292**, 1525-1528 (2001).
2 Ozawa, S. *et al.* Detection and monitoring of ongoing aseismic slip in the Tokai region, Central Japan. *Science* **298**, 1009-1012, doi:10.1126/science.1076780 (2002).
3 Lowry, A. R., Larson, K. M., Kostoglodov, V. & Bilham, R. Transient fault slip in Guerrero, southern Mexico. *Geophys. Res. Lett.* **28**, 3753-3756 (2001).
4 Douglas, A., Beavan, J., Wallace, L. & Townend, J. Slow slip on the northern Hikurangi subduction interface, New Zealand. *Geophysical Research Letters* **32** (2005).
5 Hirose, H., Hirahara, K., Kimata, F., Fujii, N. & Miyazaki, S. A slow thrust slip event following the two 1996 Hyuganada earthquakes beneath the Bungo Channel, southwest Japan. *Geophysical Research Letters* **26**, 3237-3240 (1999).
6 Schwartz, S. Y. & Rokosky, J. M. Slow slip events and seismic tremor at circum-pacific subduction zones. *Reviews of Geophysics* **45**, 32, doi:Rg3004 10.1029/2006rg000208 (2007).
7 Burgmann, R. The geophysics, geology and mechanics of slow fault slip. *Earth and Planetary Science Letters* **495**, 112-134, doi:10.1016/j.epsl.2018.04.062 (2018).
8 Ide, S., Beroza, G. C., Shelly, D. R. & Uchide, T. A scaling law for slow earthquakes. *Nature* **447**, 76-79, doi:10.1038/nature05780 (2007).
9 Gao, H. Y., Schmidt, D. A. & Weldon, R. J. Scaling Relationships of Source Parameters for Slow Slip Events. *Bulletin of the Seismological Society of America* **102**, 352-360, doi:10.1785/0120110096 (2012).
10 Peng, Z. G. & Gomberg, J. An integrated perspective of the continuum between earthquakes and slow-slip phenomena. *Nature Geoscience* **3**, 599-607, doi:10.1038/ngeo940 (2010).
11 Kanamori, H. & Brodsky, E. E. The physics of earthquakes. *Reports on Progress in Physics* **67**, 1429-1496 (2004).
12 Kanamori, H. & Anderson, L. Theoritical basis of some empirical relations in seismology. *Bull. Seism. Soc. Am.* **65**, 1073-1095 (1975).
13 Gomberg, J., Wech, A., Creager, K., Obara, K. & Agnew, D. Reconsidering earthquake scaling. *Geophysical Research Letters* **43**, 6243-6251, doi:10.1002/2016gl069967 (2016).
14 Ben-Zion, Y. H. Episodic tremor and slip on a frictional interface with critical zero weakening in elastic solid. *Geophysical Journal International* **189**, 1159-1168, doi:10.1111/j.1365-246X.2012.05422.x (2012).
15 Hawthorne, J. C. & Bartlow, N. M. Observing and Modeling the Spectrum of a Slow Slip Event. *Journal of Geophysical Research-Solid Earth* **123**, 4243-4265, doi:10.1029/2017jb015124 (2018).
16 Romanet, P., Bhat, H. S., Jolivet, R. & Madariaga, R. Fast and Slow Slip Events Emerge Due to Fault Geometrical Complexity. *Geophysical Research Letters* **45**, 4809-4819, doi:10.1029/2018gl077579 (2018).
17 Ide, S. A Brownian walk model for slow earthquakes. *Geophysical Research Letters* **35**, doi:10.1029/2008gl034821 (2008).
18 Michel, S., Gualandi, A. & Avouac, J.-P. Interseismic Coupling and Slow Slip Events on the Cascadia Megathrust. *Pure and Applied Geophysics* **2018**, doi:doi.org/10.1007/s00024-018-1991 (2018).
19 Rogers, G. & Dragert, H. Episodic tremor and slip on the Cascadia subduction zone: The chatter of silent slip. *Science* **300**, 1942-1943 (2003).
20 Obara, K., Hirose, H., Yamamizu, F. & Kasahara, K. Episodic slow slip events accompanied by non-volcanic tremors in southwest Japan subduction zone. *Geophysical Research Letters* **31**, doi:L23602 10.1029/2004gl020848 (2004).
21 Madariaga, R. in *Encyclopedia of Complexity and System Science* (ed Meyers R.) 2581–2600 (Springer, 2009).
22 Denolle, M. A. & Shearer, P. M. New perspectives on self-similarity for shallow thrust earthquakes. *Journal of Geophysical Research-Solid Earth* **121**, 6533-6565, doi:10.1002/2016jb013105 (2016).
23 Bartlow, N. M., Miyazaki, S., Bradley, A. M. & Segall, P. Space-time correlation of slip and tremor during the 2009 Cascadia slow slip event. *Geophysical Research Letters* **38**, doi:10.1029/2011gl048714 (2011).
24 Wech, A. G. & Bartlow, N. M. Slip rate and tremor genesis in Cascadia. *Geophysical Research Letters* **41**, 392-398, doi:10.1002/2013gl058607 (2014).
25 Galetzka, J. *et al.* Slip pulse and resonance of the Kathmandu basin during the 2015 Gorkha earthquake, Nepal. *Science* **349**, 1091-1095, doi:10.1126/science.aac6383 (2015).

26 Gao, X. & Wang, K. L. Rheological separation of the megathrust seismogenic zone and episodic tremor and slip. *Nature* **543**, 416-+, doi:10.1038/nature21389 (2017).
27 Scholz, C. H. *The mechanics of earthquakes*. (Cambridge Universtity Press, 1990).
28 Noda, H., Lapusta, N. & Kanamori, H. Comparison of average stress drop measures for ruptures with heterogeneous stress change and implications for earthquake physics. *Geophysical Journal International* **193**, 1691-1712, doi:10.1093/gji/ggt074 (2013).
29 Meade, B. J. Algorithms for the calculation of exact displacements, strains, and stresses for triangular dislocation elements in a uniform elastic half space. *Computers & Geosciences* **33**, 1064-1075, doi:10.1016/j.cageo.2006.12.003 (2007).
30 Schmidt, D. A. & Gao, H. Source parameters and time-dependent slip distributions of slow slip events on the Cascadia subduction zone from 1998 to 2008. *Journal of Geophysical Research-Solid Earth* **115**, doi:10.1029/2008jb006045 (2010).
31 Wech, A. G., Creager, K. C., Houston, H. & Vidale, J. E. An earthquake-like magnitude-frequency distribution of slow slip in northern Cascadia. *Geophysical Research Letters* **37**, doi:10.1029/2010gl044881 (2010).
32 Obara, K. Phenomenology of deep slow earthquake family in southwest Japan: Spatiotemporal characteristics and segmentation. *Journal of Geophysical Research-Solid Earth* **115**, doi:10.1029/2008jb006048 (2010).
33 Kanamori, H. & McNally, K. C. Variable rupture mode of the subduction zone along the Ecuador-Colombia coast. *Bulletin of the Seismological Society of America* **72**, 1241-1253 (1982).
34 Thatcher, W. Order and diversity in the modes of Circum-Pacific earthquake recurrence. *J. Geophys. Res.* **95**, 2609-2623 (1990).
35 Radiguet, M. *et al.* Spatial and temporal evolution of a long term slow slip event: the 2006 Guerrero Slow Slip Event. *Geophysical Journal International* **184**, 816-828, doi:10.1111/j.1365-246X.2010.04866.x (2010).
36 Ide, S. Variety and spatial heterogeneity of tectonic tremor worldwide. *Journal of Geophysical Research-Solid Earth* **117**, doi:10.1029/2011jb008840 (2012).
37 Aki, K. Maximum Likelihood estimate of b in the formula $\log N = a - bM$ and its confidence limits. *Bull. Earthquake Res. Inst.* **43**, 237-239 (1965).

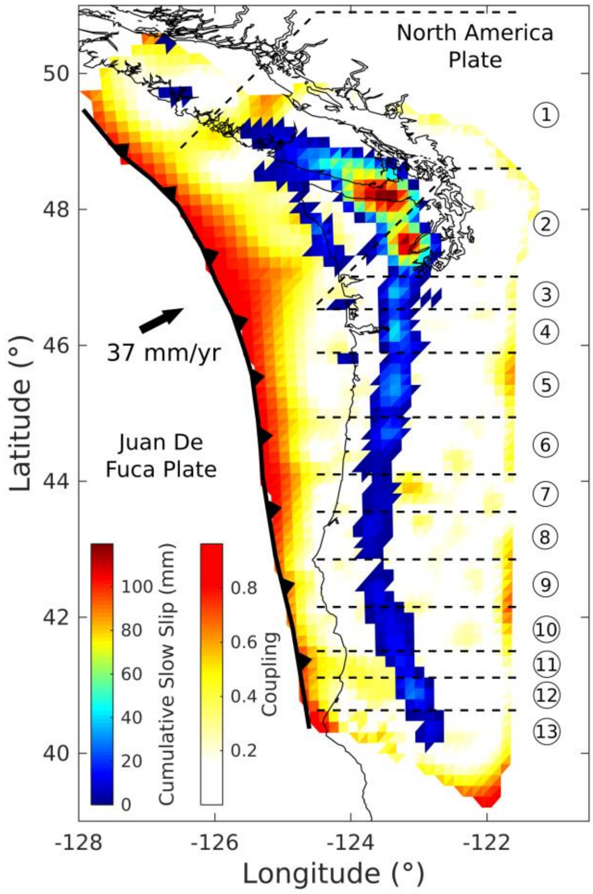

Figure 1 | Comparison of interseismic coupling with cumulated slip due to episodic slow slip between 2007 and 2017[18]. The analysis is based on GPS time series between 2007.000 and 2017.632 from 352 cGPS stations from the Pacific Geodetic Array (PANGA) and the Plate Boundary Observatory (PBO). SSEs were determined from the temporal variations of geodetic displacement, corrected for hydrological effects and other tectonic sources (co- and post-seismic deformations). The cumulated slip due to all the 64 SSEs in our catalog forms a band that follows the intersection of the forearc Moho with the megathrust and is disconnected from the shallower locked portion of the megathrust. Interseismic coupling is defined as the rate of slip deficit due to locking of the Megathrust in the interseismic period divided by the long term slip rate. Interseismic coupling and the long term forearc motion was determined from the secular GPS velocities (best fitting linear trend to the GPS time series). The model shown here assumes locking at the trench. Alternative models assuming no locking at the trench can fit the data equally well but, in any case, the locked zone is clearly disconnected from the zones of episodic slow slip and tremors[26].

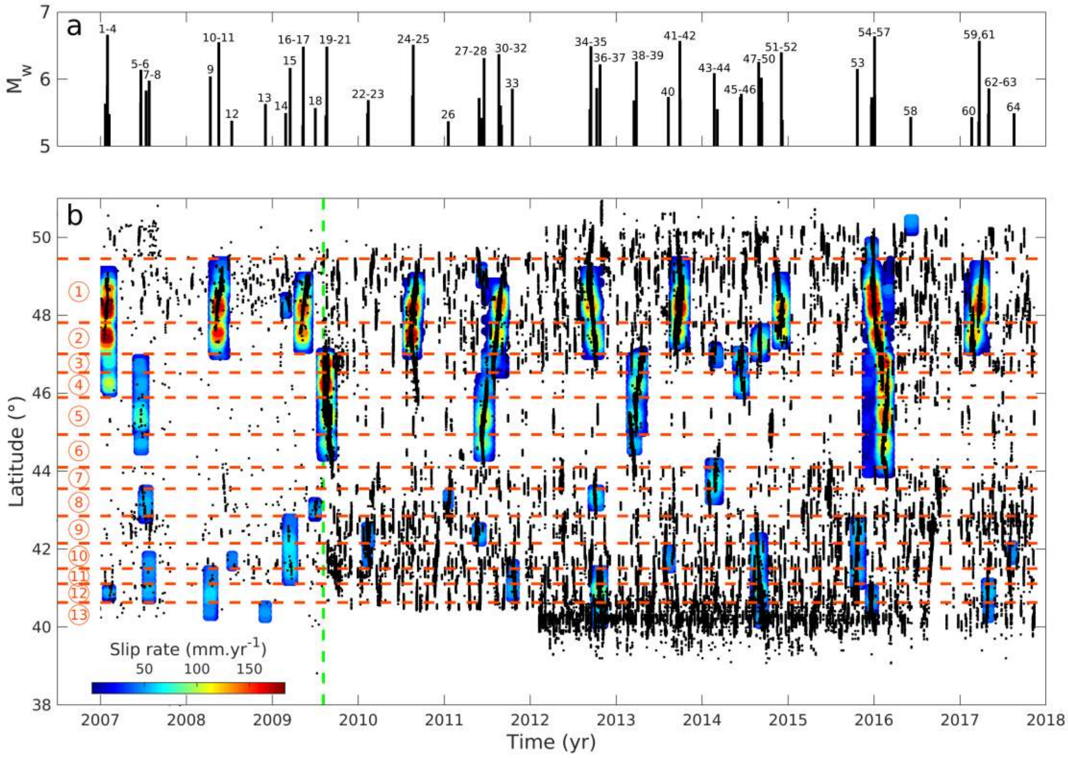

Figure 2 | Spatio-temporal distribution of slip and SSEs segmentation. a) Time line with magnitudes, labeled by event number, of all 64 SSEs of our original catalog[18]. b) Timing and rupture extent of the SSEs. The black dots indicate tremors. The catalogue from Ide[36] is used until 2009.595, the catalogue from PNSN (https://pnsn.org/tremor) is used thereafter. The vertical green line marks the separation between the two catalogs. The dashed pink lines indicate the segment boundaries defined as the rupture ends (see also Supplementary Fig. S3).

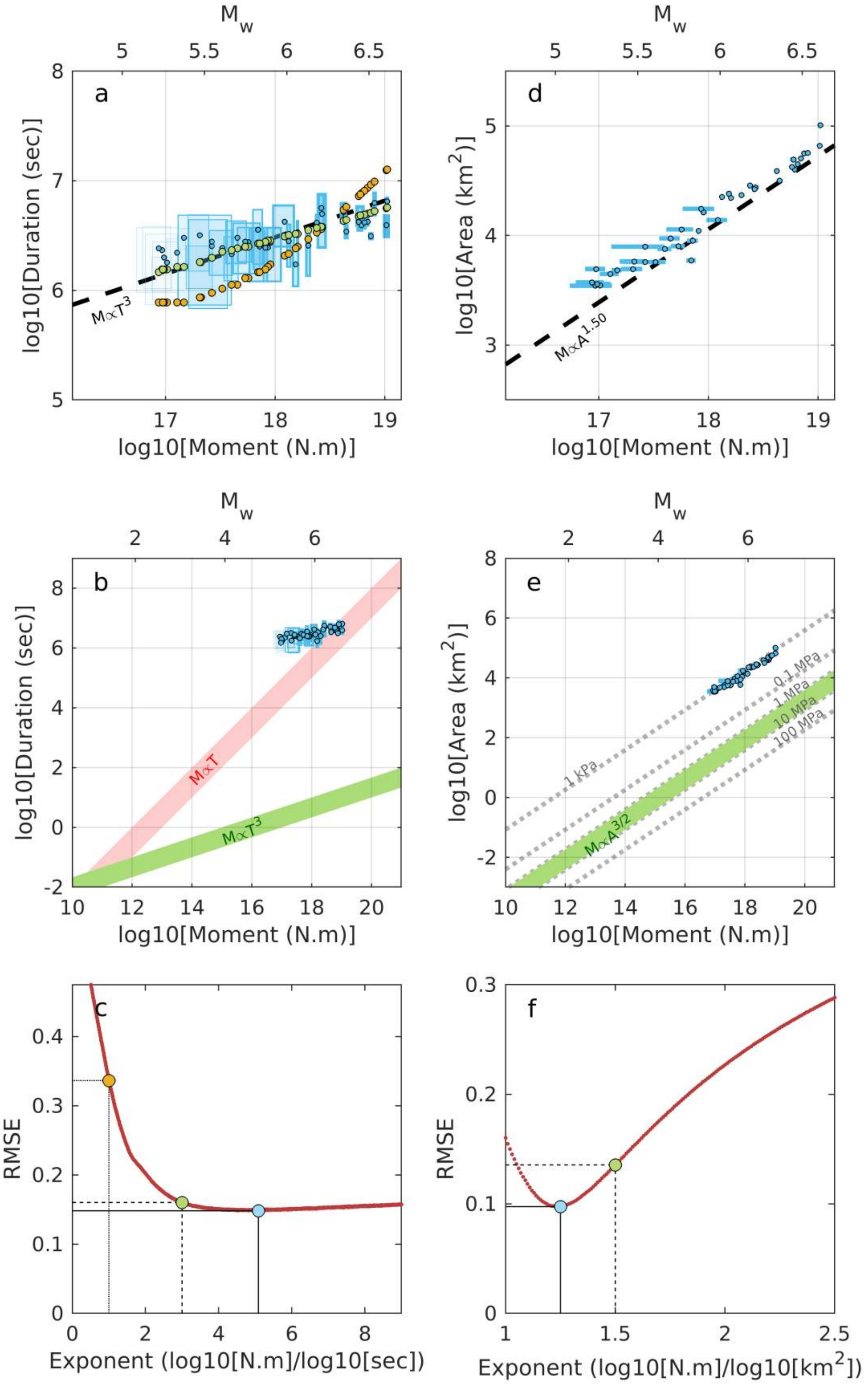

Figure 3 | Moment-Duration and Moment-Area scaling laws. (a) Relationship between the moment, M_0, released by SSEs and their duration, T. The black dashed line indicates the slope of the scaling law for regular earthquakes. The green and yellow dots (as in Fig. 3c) show the expected moment-duration distribution for catalogs following $M_0 \propto T^3$ and $M_0 \propto T$, respectively, affected by the temporal filter in the case of the best-fitting value of the intercept. (b) Comparison with the scaling laws for slow (red shading) and regular earthquakes (green shading) proposed by Ide et al.[8]. (c) Data fit assuming $M_0 \propto T^c$, taking into account the magnitude and duration uncertainties and the effect of the temporal filter (see Methods). The RMSE for *c*=3 (green dot) is half that for *c*=1 (yellow dot), and only 10% larger than the best fitting value which is obtained for *c*=5.09 (blue dot). (d) Relationship between the moment released by SSEs and their rupture area, A. The black dashed line indicates the scaling law for regular earthquakes. (e) Comparison with the scaling law of regular earthquakes (green shading). Stress drop iso-lines are estimated based on the circular crack model[12]: $M_o = C^{-1}\Delta\tau A^{3/2}$, $\Delta\tau$ the stress drop, A the rupture area and C=2.44. See supplement for details about the measurements. (f) Data fit assuming $M_0 \propto A^{\mathrm{d}}$, taking into account the uncertainty on moment (see Methods). The best fitting value is *d*=1.25.

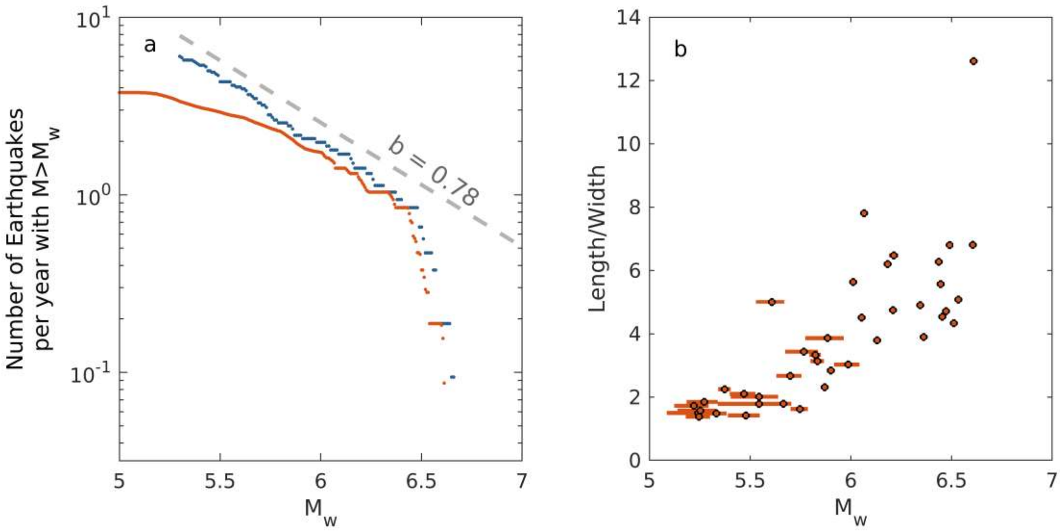

Figure 4 | Frequency-Magnitude distribution and aspect ratio of SSEs in Cascadia. *(a)* Logarithm of the number of SSEs with moment magnitude larger than the value in abscissa using the original catalog[18] (blue dots) and the revised catalog (red dots). Like regular earthquakes, SSEs are observed to follow approximately a linear trend, i.e. the Gutenberg-Richter relationship (see Methods for the b-value estimate). The apparent larger *b*-value at M_w>6.4 is defined by only 11 events and could suggest that the distribution is truncated possibly as result of the along-strike segmentation. (b) Aspect ratio of rupture areas. See supplements for details about area and aspect ratio measurements.

METHODS

Moment-duration scaling

We determine the best fitting moment-duration scaling law, $Log10(T) = \left(\frac{1}{c}\right) Log10(M_0) + b$, taking into account the uncertainties on SSEs duration and moment (see supplement) and the effect of the temporal filter. We grid search for the best exponent, c, and intercept, b, of the scaling law. For each pair of exponent and intercept values, 1500 random catalogs of 40 SSEs are created assuming a uniform probability between the minimum and maximum moment and duration values. We then compare these catalogs with the moment-duration of synthetic catalogues. The events in the synthetic catalogs have the same magnitudes as in the random catalog, thus the same final moment released, M_S, but a duration, D_s, prescribed by the tested scaling law. To account for the filter we generate synthetic time series assuming boxcar moment rate function with a moment rate equal to M_S/D_s during the event (and 0 N.m/day otherwise). We apply the same filter as to the real data, (a zero-phase digital filtering using a 5-day window), and estimate durations from the filtered moment rate functions (we take a moment rate threshold of $\dot{M}_{0\ thresh} =$ 6.63 N.m/day equivalent to the case of the fault smallest patch slipping at 40 mm/yr with a shear modulus $\mu = 30GPa$). Finally, for the tested exponent and intercept, the RMSE is calculated between the durations of the 40 x 1500 produced events and their associated smoothed synthetics. The range of values explored for the intercept and exponent spans from -35 to 7 log10[sec] and 0.5 to 9 log10[N.m]/log10[sec], respectively, using a step of 0.01 for both. The minimum RMSE for each tested exponent is shown in Fig. 3c and the best fitting corresponds to c= 5.09 but is only ~8% smaller than the RMSE obtained for c=3 .

Moment-area scaling

We use a similar procedure to search for the best fitting moment-area scaling law, $Log10(A) = \left(\frac{1}{d}\right) Log10(M_0) + r$, taking into account SSE's moment uncertainties. We grid search for the best exponent, d, and intercept, r. For each pair of tested exponent and intercept, 1500 random catalogs of 40 SSEs are created, assuming a uniform probability distribution between the estimated minimum and maximum moments and areas. For each of these catalogs, an associated synthetic catalogue was created with areas prescribed to follow the tested scaling law. For each tested exponent and intercept, a RMSE is then calculated between the areas of the 40 x 1500 produced events and their associated synthetics. The tested values of the intercept and exponent range from -15 to -1.5 log10[km^2] and from 1 to 2.5 log10[N.m/km^2], respectively, using a step equal to 0.01 for both. The minimum RMSE for each exponent tested is shown in Fig. 3f and the best fit corresponds to an exponent equal to 1.25.

Measurement of SSE rupture area and aspect ratio.

The SSEs rupture areas are defined as the sum of the sub-faults areas which experienced $\dot{\delta}_{deficit} < V_{thresh}$[18], extended to their neighboring sub-faults, based on the $\sim$30 days filtered $\dot{\delta}_{deficit}$. We thus estimate the SSEs length and width relative to a mean strike line that follows approximately the curved geometry of the Megathrust and runs through the middle of cumulated slip distribution of SSEs (Fig. S4). For each SSE, the rupture length is defined as the distance between the northern and southern intersections between the rupture's outline and the mean strike line. The width is defined as twice the mean distance between the rupture's outline and the mean strike line. Because some SSE ruptures are not centred over it or might not even cut it, we shift the mean strike line along dip for each SSE, forcing it to pass through its slipping area where the measured length is maximum.

Note that the SSEs spatio-temporal extension is sensitive to the inversion regularisation, the temporal filter applied to $\delta_{deficit}$, and the chosen value for V_{thresh}.

Determination of Magnitude-Frequency distribution

The magnitude frequency distribution for the revised catalog in Figure 4a is calculated taking into account the SSEs magnitude uncertainties calculated in the supplementary section '*Measurements of SSE duration and moment release'*. We assume that each event has a uniform distribution within its moment uncertainty and sum all of those distributions. The resulting Probability Density Function (PDF), P_{events}, gives the number of events per magnitude. We then calculate for each magnitude tested, M_{test}, the number of events over M_{test} per year:

$N = \int_{M_{test}}^{\infty} P_{events}(M_w)\, dM_w$ .The b-value of the Gutenberg-Richter distribution that best fits the original catalog (64 events) is estimated to 0.78 using the maximum likelihood method[37]. We do not estimate the b-value for the revised catalog due to the rollover at lower magnitudes due to the data selection.

SUPPLEMENTS

Measurements of SSE duration and moment release

In our original study[18], we applied an equiripple low-pass filter to the slip deficit, $\delta_{deficit}$, with passband frequency of 1/21 days^{-1}, stopband of 1/35 days^{-1}, passband ripple of 1dB with 60dB of stopband attenuation. Calling $\dot{\delta}_{deficit}$ the slip rate deficit on the megathrust with respect to the long-term creep, SSEs are detected when $\dot{\delta}_{deficit}(p,t) < V_{thresh}$, where V_{thresh} corresponds to a slip deficit rate threshold set to -40 mm/yr. The applied filter removes any

SSE with a duration under 3 weeks and bias the estimation of the start and end of moderate SSEs, thus their duration.

To attenuate the duration estimation bias of the SSEs detected by the method described above, we proceed as follows. For each SSE, we focus only in the area as defined by the previous filter. Starting from the first automatic detection [t'_{start}, t'_{end}], we consider an enlarged time span [t_{start}, t_{end}] = [t'_{start} – 35 days, t'_{end} + 35 days]. Instead of applying a low-pass filter, which truncates all events with frequency higher than the specified passband frequency, we perform a zero-phase digital filtering on the rough $\delta_{deficit}$ using a 5-day window. The filter is an averaging sliding window which passes through the data in the forward and reverse direction. As a result, the time shift is zero and periods shorter than 9 days are filtered out. We then convert $\delta_{deficit}$ into moment deficit, $M_{0deficit}$, taking a shear modulus $\mu = 30\ GPa$ and calculate the moment deficit rate, $\dot{M}_{0deficit}$, by taking the derivative in time. The derivative is taken using 1 day time steps. Note that, even by focusing directly on a specified SSE area, it is not possible to detect the onset and end of a SSE by looking at its global moment rate function obtained as the integral of the moment rate over all the selected sub-faults. Indeed, the onset of a SSE can be masked by neighbouring sub-faults with positive $\dot{M}_{0deficit}$ (associated with loading). It is thus important to look at sub-faults individually to detect the onset and end of a SSE.

The complex $\dot{M}_{0deficit}$ signal of each sub-fault makes it very difficult to establish an automated detection of the SSEs' time-boundaries, and we thus base ourselves on two manual methods to estimate the onset and end of SSEs, the two methods providing a minimum and maximum duration estimation. 1) The first method, which provides the minimum duration estimation, consists in a) taking a slip deficit rate threshold, V_{thresh}, set to -40 mm/yr, b) calculating for each sub-fault its equivalent moment rate, $\dot{M}_{0\,thresh}$, since the sub-faults have different areas, and c) determining the timing of the first and last sub-fault with $\dot{M}_0 < \dot{M}_{0\,thresh}$. This method is generally straight forward but provides a SSE duration underestimation since the event could well be continuing but with moment rates under $\dot{M}_{0\,thresh}$. In several cases the sub-faults moment rates present several peaks oscillating around $\dot{M}_{0\,thresh}$ (e.g., SSEs #33, supplementary document). In such cases we generally pick the duration on the most plausible peak related to the SSE (even if the other peaks might be part of the SSE) aiming in doing so to provide an absolute lower limit of the duration. 2) The second method, which provides the maximum duration estimation, is an estimation of the timing of the first and last subfault when $\dot{M}_0 < 0$. However, due to the noise in the slip time series, there is no simple way to determine this timing. We choose to consistently take the onsets and end of SSEs that determine their maximum duration possible regarding the data available, at the risk sometimes to add noise within the time-boundaries. The two described methods serve as guidelines and provide a bracket on SSEs' duration. An example of duration estimation is shown in Fig. S3 for SSE 34. The SSEs estimated onset and end times are provided in Table S1 and shown in the supplementary document, which contains also the explanation of each events picking.

The bracket on SSEs' duration also provides a bracket on their moment release. The total moment release, M_o^{Total}, of a SSE is defined as:

$$M_o^{Total} = \sum_{p=1}^{Q} M_0^p(T_{end}) - \sum_{p=1}^{Q} M_0^p(T_{start}),$$

where Q is the total number of sub-faults involved in the SSE, $M_0^p(t)$ is the cumulative moment released by patch p at time t, and T_{start} and T_{end} are the SSE onset and end times as determined by the 2 methods mentioned above. An example of the procedure is shown for SSE 34 in Fig. S3b.

Moment, duration and area biases, and comparison with SSEs from the literature.

Various sources of bias were affecting our initial catalog[18]. Biases in the duration estimation due to automatic picking of the onset and end of each SSE and to the temporal filtering were alleviated with the manual picking method described above and by accounting for the filtering effect in the determination of the best fitting scaling law (Methods). The duration estimations depend also on the initial slip rate detection threshold of SSEs[18] which determines the SSEs areas.

Biases on SSEs areas might originate from both the slip inversion regularization[18] and the SSEs slip rate detection threshold, V_{thresh} (see supplement *Measurements of SSE duration and moment release* and *Measurements of SSE rupture area and aspect ratio*). The detection threshold method tends to underestimate areas since sub-faults could well be part of a SSE but have slip rates under V_{thresh}. Lowering V_{thresh} would enlarge the rupture areas and increase the noise level. Note that the detection threshold bias is also dependent on the temporal filter applied on the initial slip deficit for the SSEs detection[18] (filter with a passband frequency of 1/21 days^{-1}, stopband of 1/35 days^{-1}, passband ripple of 1dB with 60dB of stopband attenuation).

Moment estimation biases are also linked to the biases mentioned above since they are estimated based on the SSEs onset and end time (see supplement *Measurements of SSE duration and moment release*), and depend on the SSEs area estimation too.

There are three common events in the SSE catalogs of Michel et al.[18] and Schmidt and Gao[30]. These three events have similar magnitudes and similar distributions (Fig. S5). The peak slip estimated by Michel et al. [18] are half those of Schmidt and Gao[30] though. This is probably because the solutions of Michel et al.[18] are more strongly regularized (resulting in smoother slip distributions) and do not include inter-SSE-loading. The slip potencies (the integral of slip over rupture area) agree within 30% between the two studies. Note also that Michel et al. [18] uses an elastic modulus of 30GPa instead of 50GPa in Schmidt and Gao[30], and that the SSE areas are determined differently in the two studies.

Comparison of tremors durations[13] and SSE durations from geodesy (this study).

We compared the SSEs duration that we measured based on the GNSS times series with the duration derived from the tremors[13]. We used revised time picks of the onset and end of the tremors provided by Gomberg (personal communication). For these common events the durations derived from the tremors and from geodesy are consistent given the effect of the filtering (Fig. S6).

Supplementary Figures and Table

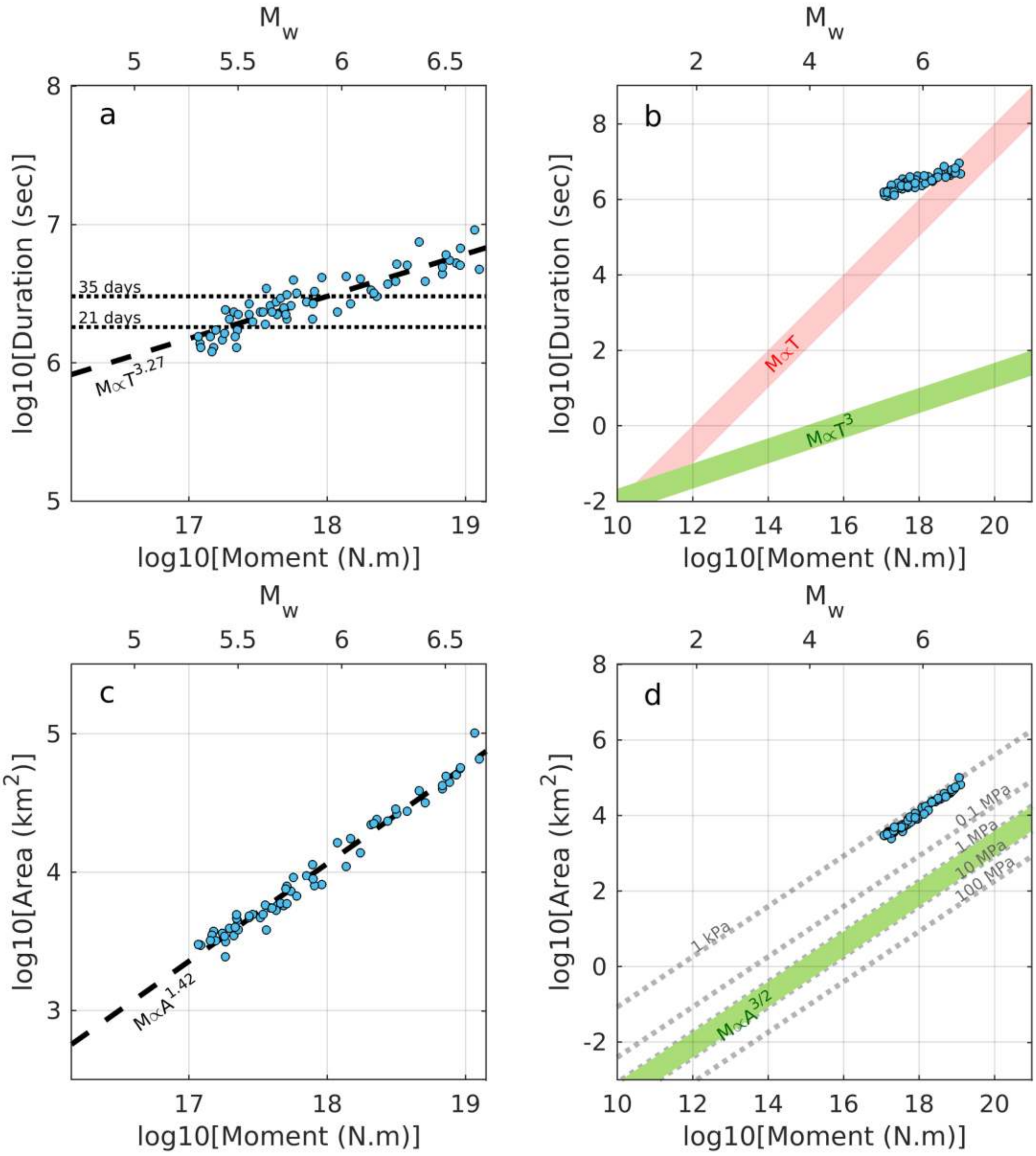

Figure S1 | Moment-Duration and Moment-Area scaling laws for automatic measurements. (a) Relationship between the moment released by SSEs and their duration. The black dashed line shows the best linear fit. The two horizontal dotted lines indicate the filter passband and stopband values, 21 and 35 days respectively, used on the $\delta_{deficit}$ in Michel et al.[18] (b) Comparison with the scaling laws for slow (red shading) and regular earthquakes (green shading) proposed by Ide et al.[6]. (c) Relationship between the moment released by SSEs and their rupture area. The black dashed line shows the best linear fit. (d) Comparison with the scaling laws regular earthquakes (green shading). Stress drop iso-lines estimated based on the circular crack model.

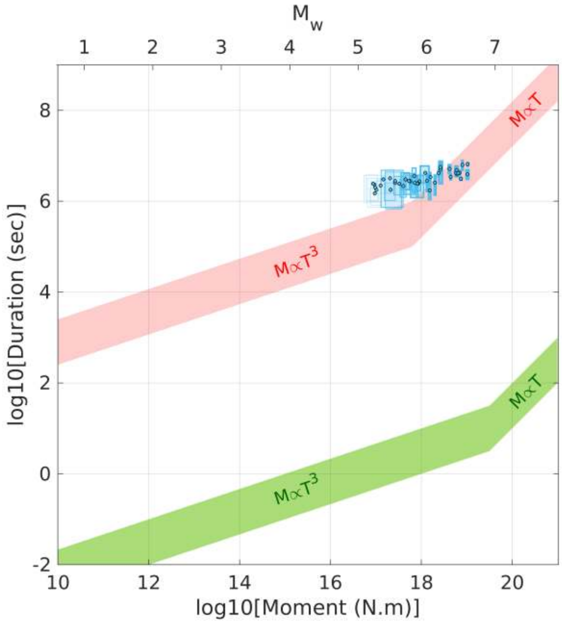

Figure S2 | Moment-Duration scaling law comparison with Gomberg et al.[12] theory. Comparison of the moment-duration scaling of SSEs in Cascadia with the trends proposed for unbounded $M_0 \propto T^3$ and bounded $M_0 \propto T$ ruptures by Gomberg et al.[12] for seismic slip (green shading) and slow slip (red shading). Here we are plotting only our manual measurements (blue dots and boxes).

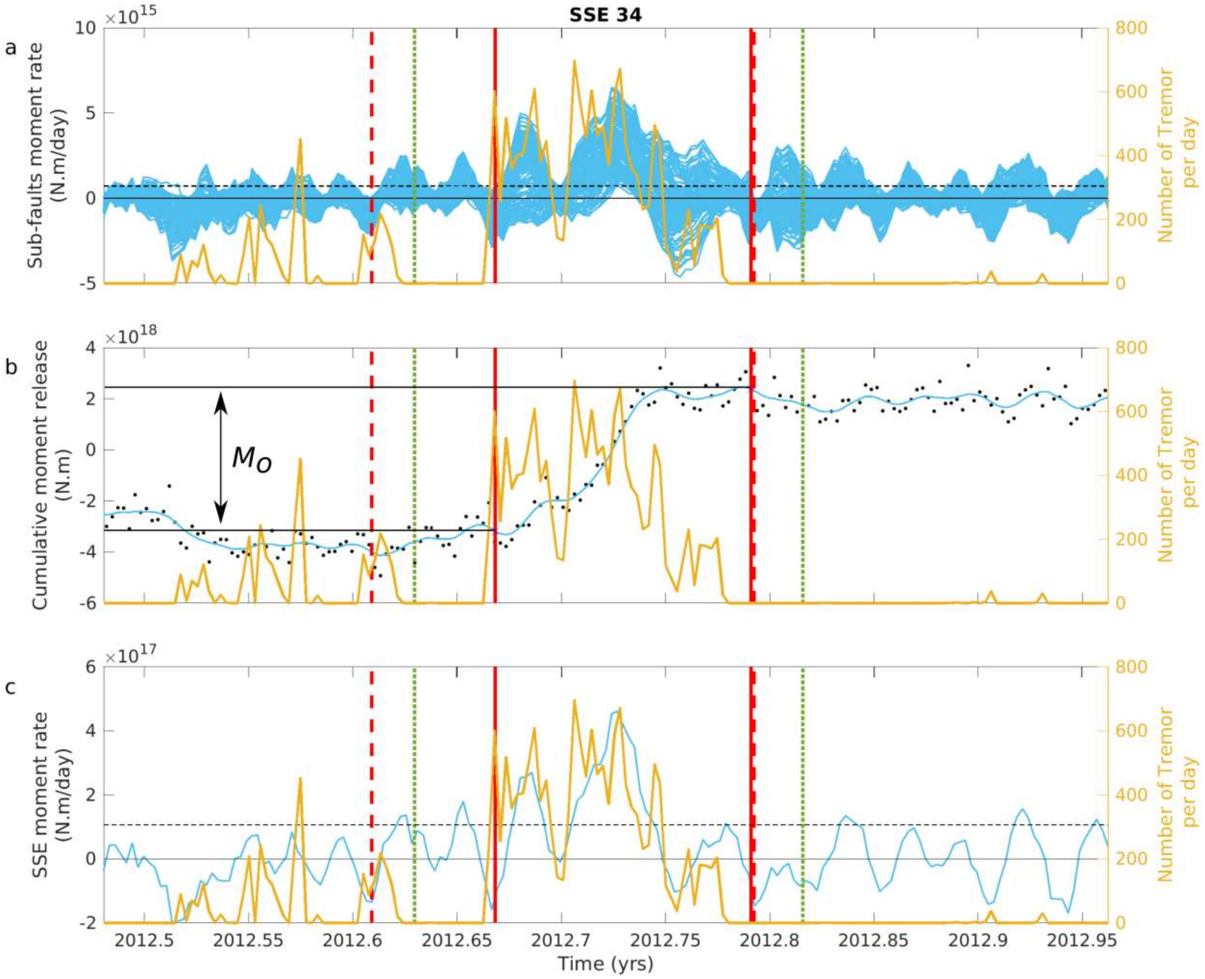

Figure S3 | SSEs duration estimations – SSE 34 example. (a) The blue lines show the SSEs sub-faults moment rate curves after a zero-phase digital filtering on the rough $\delta_{deficit}$ using a 5-day window (effectively 9 days). The dotted yellow line shows the number of tremors per day within the SSE rupture area. The solid red lines indicate the start and end times picked manually to estimate the minimum duration. They are determined by the timing of the first and last sub-fault with $\dot{M}_{0\,deficit} < \dot{M}_{0\,thresh}$, (the threshold rate is represented by the horizontal black dashed line). The dashed red lines indicate similarly the SSEs start and end times picked to estimate the maximum duration. They are determined by the times of the first and last sub-fault when $\dot{M}_{0\,deficit} < 0$. The dotted green lines indicate the SSEs start and end automatic time picks[18]. (b) The black dots show the cumulative moment release in excess of the moment release that would have accumulated at the interseismic rate (since the SSE are extracted from the time series corrected for long term interseismic strain). The blue line is its smoothed version using the same filter as indicated in (a). The red, yellow, and green lines are the same as in (a). To illustrate the methodology used to calculate the SSE moment release, M_0, we indicate the values taken for the calculation based on the minimum duration by two horizontal solid black lines. (c) The blue line indicates the SSE moment rate (sum of the SSE sub-faults moment rate). The horizontal dashed black line represents the $\dot{M}_{0\,thresh}$ sum of all the sub-faults. The red, yellow, and green lines are the same as in (a).

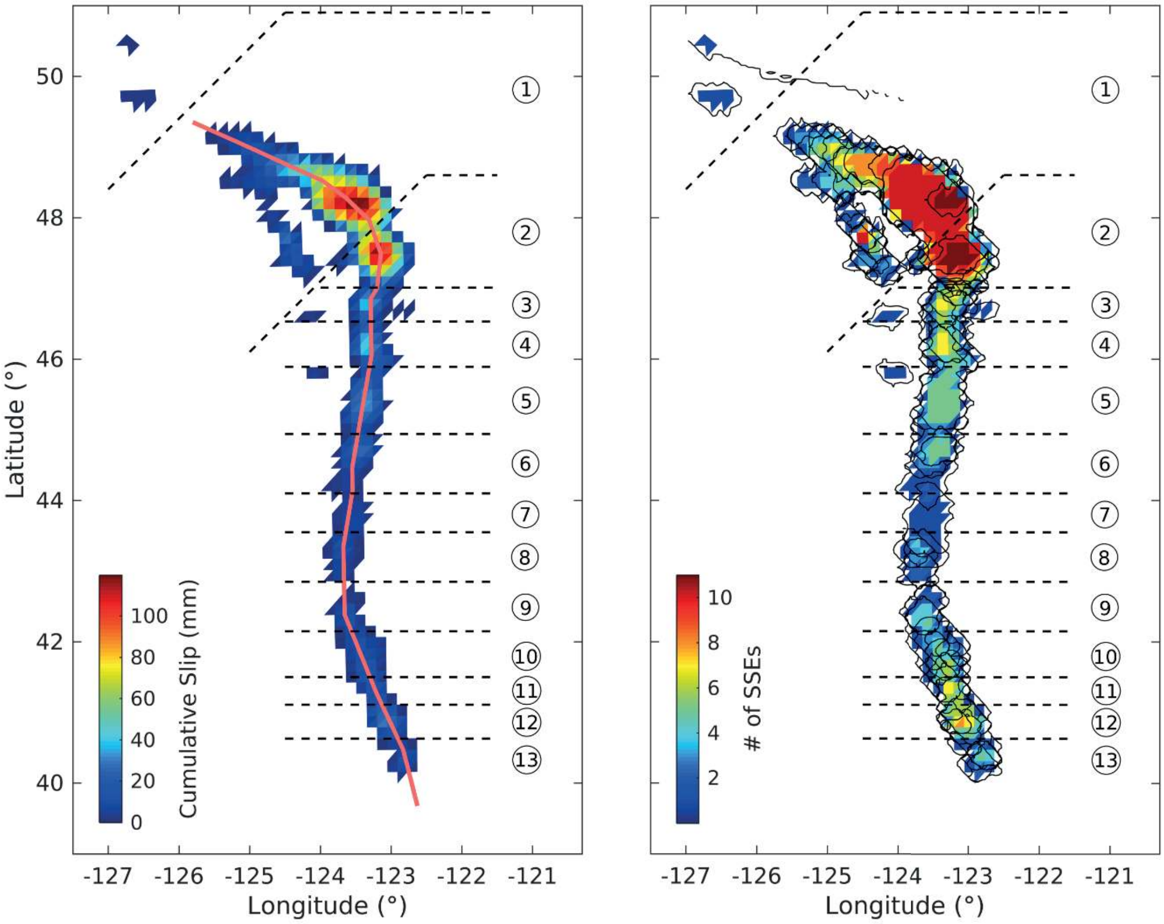

Figure S4 | Segments delimitation. (a) SSEs cumulative slip. The pink line indicates a representative line of the average along-strike location of SSEs given by Michel et al. [18] (b) Map indicating the number of times a sub-fault has experienced a SSE. The black contours delimit the extent of each SSE. The dashed black lines in (a) and (b) correspond to the selection of asperities.

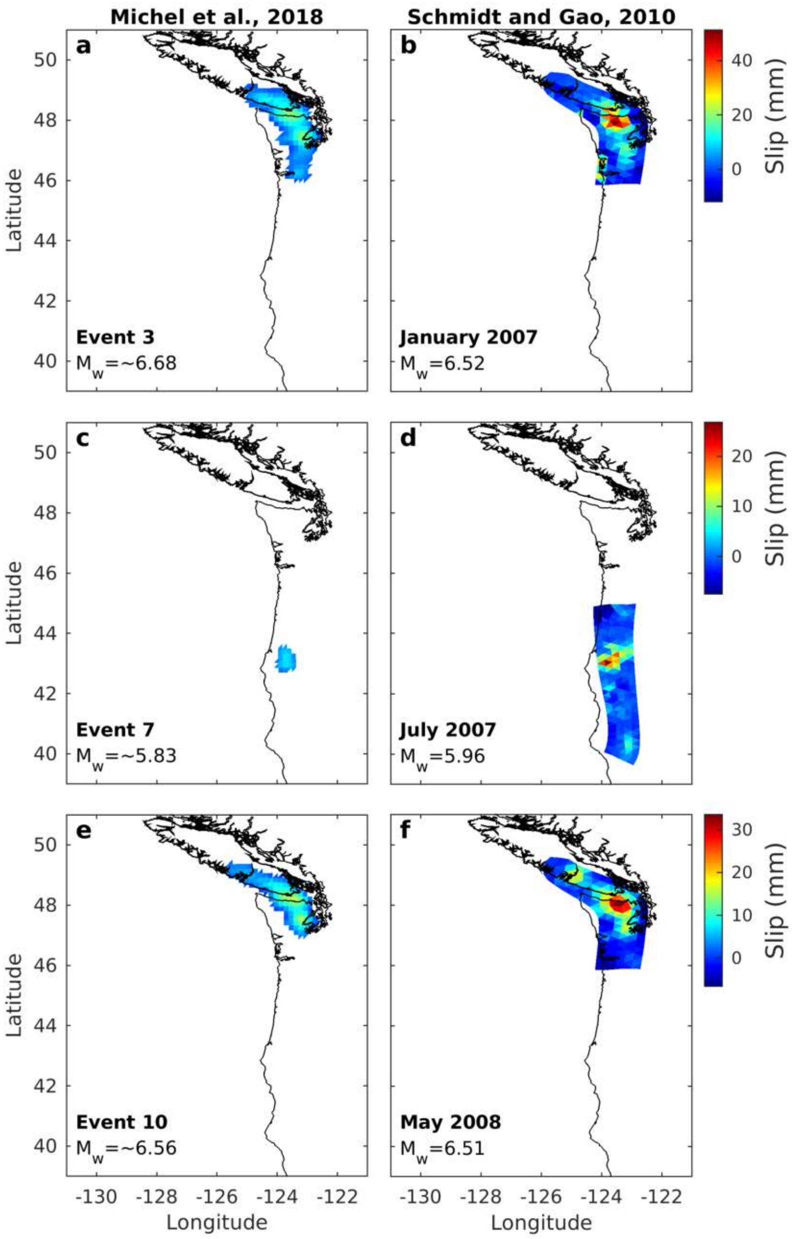

Figure S5 | Comparison with slip models of Schmidt and Gao[30]. (a), (c) and (e) are the cumulative slip models for SSEs #3, 7 and 10 of Michel et al.[18]. (b), (d) and (f) are the cumulative slip models of the same SSEs estimated by Schmidt and Gao[30]. The magnitudes indicated in all panels are calculated taking a shear modules $\mu = 30$ GPa.

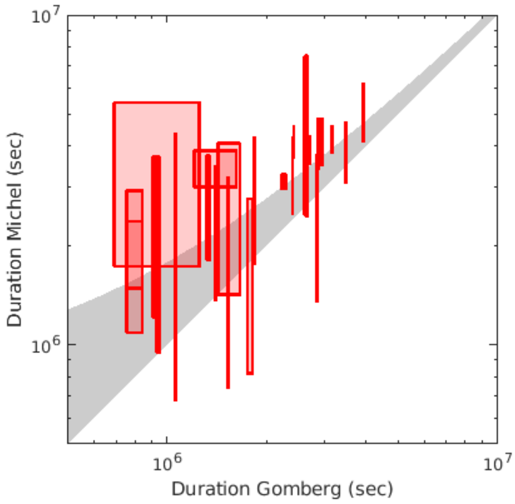

Figure S6 | Comparison for tremors durations[13] and SSE durations derived from geodesy. The comparison is done for 24 common events. The uncertainties for the duration on the y-axis are given by our minimum/maximum duration estimations. The uncertainties on the x-axis are given by the minimum/maximum durations using entire/abbreviated tremor cluster catalogs (see Gomberg et al.[13]). The lower boundary of the grey shaded area corresponds to a perfect fit. The upper boundary takes into account the ~9 days period cut-off of the filter.

Table S1 | SSEs duration manual estimation. The start and end time pick for the minimum duration estimation are determined by the timing of the first and last sub-fault with $\dot{\delta}_{deficit} < V_{thresh}$. The start and end time pick for the maximum duration estimation are determined by the timing of the first and last sub-fault when $\dot{\delta}_{deficit} < 0$. The SSEs durations reported here are affected by the ~9 days filter bias *(*see supplement *Measurements of SSE duration and moment release).*

SSE #	Start (Max Duration)	Start (Min Duration)	End (Min Duration)	End (Max Duration)
3	2007.0267	2007.0294	2007.128	2007.1773
4	2007.0294	2007.0733	2007.1034	2007.1472
5 & 6	2007.422	2007.4264	2007.5058	2007.5579
7	2007.4576	2007.4839	2007.5397	2007.5934
8	2007.491	2007.5318	2007.5852	2007.6099
9	2008.2286	2008.2642	2008.3025	2008.3464
10	2008.316	2008.3265	2008.4477	2008.4627
12	2008.4969	2008.5298	2008.5626	2008.6174
13	2008.8939	2008.924	2008.9569	2008.9745
14	2009.1266	2009.166	2009.213	2009.2197
15	2009.1759	2009.179	2009.2135	2009.251
16	2009.3183	2009.3238	2009.436	2009.4552
18	2009.429	2009.485	2009.5325	2009.5839
19	2009.5579	2009.587	2009.6989	2009.7125
22 & 23	2010.067	2010.0921	2010.1355	2010.178
24	2010.5859	2010.5887	2010.7064	2010.7324
26	2010.9993	2011.0431	2011.069	2011.087
27	2011.347	2011.372	2011.3936	2011.4867
28	2011.3689	2011.425	2011.5031	2011.6071
29	2011.3717	2011.4275	2011.451	2011.4747
30	2011.5305	2011.555	2011.6865	2011.7276
33	2011.7345	2011.796	2011.841	2011.864
34	2012.609	2012.6684	2012.791	2012.7926
36	2012.7242	2012.7269	2012.7844	2012.843
37	2012.7445	2012.7998	2012.8429	2012.8638
38 & 39	2013.1403	2013.1814	2013.305	2013.3758
40	2013.5401	2013.562	2013.5852	2013.6934
41	2013.6769	2013.682	2013.776	2013.781
43	2014.0274	2014.1314	2014.2108	2014.216
44	2014.119	2014.1218	2014.1971	2014.2357
45 & 46	2014.333	2014.438	2014.4928	2014.5051
47 & 50	2014.5914	2014.6051	2014.7135	2014.746
48	2014.6215	2014.6516	2014.69	2014.7392
51	2014.857	2014.8597	2014.955	2014.9802
53	2015.7276	2015.7851	2015.8371	2015.8535
54 & 55	2015.9521	2015.974	2016.168	2016.1711
56	2015.9202	2015.9603	2015.999	2016.0178
59	2017.039	2017.1239	2017.279	2017.2827
62 & 63	2017.2981	2017.2991	2017.3484	2017.4086

64	2017.5428	2017.5715	2017.603	2017.606